

Article

A Multimodal Desorption Electrospray Ionisation Workflow Enabling Visualisation of Lipids and Biologically Relevant Elements in a Single Tissue Section

Catia Costa ¹, Janella De Jesus ^{2,3}, Chelsea Nikula ³, Teresa Murta ³, Geoffrey W. Grime ¹, Vladimir Palitsin ¹, Véronique Dartois ⁴, Kaya Firat ⁴, Roger Webb ¹, Josephine Bunch ³ and Melanie J. Bailey ^{1,2,*}

¹ University of Surrey Ion Beam Centre, Guildford GU2 7XH, UK

² Department of Chemistry, University of Surrey, Guildford GU2 7XH, UK

³ The National Physical Laboratory, Teddington TW11 0LW, UK

⁴ Center for Discovery and Innovation, Hackensack Meridian School of Medicine, Nutley, NJ 07110, USA

* Correspondence: m.bailey@surrey.ac.uk; Tel.: +44-(0)1483682593

Abstract: The collocation of elemental species with host biomolecules such as lipids and metabolites may shed new light on the dysregulation of metabolic pathways and how these affect disease pathogenesis. Alkali metals have been the subject of extensive research, are implicated in various neurodegenerative and infectious diseases and are known to disrupt lipid metabolism. Desorption electrospray ionisation (DESI) is a widely used approach for molecular imaging, but previous work has shown that DESI delocalises ions such as potassium (K) and chlorine (Cl), precluding the subsequent elemental analysis of the same section of tissue. The solvent typically used for the DESI electrospray is a combination of methanol and water. Here we show that a novel solvent system, (50:50 (%v/v) MeOH:EtOH) does not delocalise elemental species and thus enables elemental mapping to be performed on the same tissue section post-DESI. Benchmarking the MeOH:EtOH electrospray solvent against the widely used MeOH:H₂O electrospray solvent revealed that the MeOH:EtOH solvent yielded increased signal-to-noise ratios for selected lipids. The developed multimodal imaging workflow was applied to a lung tissue section containing a tuberculosis granuloma, showcasing its applicability to elementally rich samples displaying defined structural information.

Keywords: multimodal imaging; correlative imaging; ion beam analysis; desorption electrospray ionisation mass spectrometry; biological tissue analysis



Citation: Costa, C.; De Jesus, J.; Nikula, C.; Murta, T.; Grime, G.W.; Palitsin, V.; Dartois, V.; Firat, K.; Webb, R.; Bunch, J.; et al. A Multimodal Desorption Electrospray Ionisation Workflow Enabling Visualisation of Lipids and Biologically Relevant Elements in a Single Tissue Section. *Metabolites* **2023**, *13*, 262. <https://doi.org/10.3390/metabo13020262>

Academic Editor: Michal Ciborowski

Received: 25 January 2023

Revised: 7 February 2023

Accepted: 9 February 2023

Published: 11 February 2023



Copyright: © 2023 by the authors. Licensee MDPI, Basel, Switzerland. This article is an open access article distributed under the terms and conditions of the Creative Commons Attribution (CC BY) license (<https://creativecommons.org/licenses/by/4.0/>).

1. Introduction

Our understanding of biological processes is being continuously pushed by advances in multimodal imaging or spatial “omics”, which allows for the integration of structural, molecular and elemental information [1]. Several recent reports in the literature have explored the combination of mass spectrometry imaging (MSI) with elemental mapping techniques for biological applications [2–7]. The integration of these imaging modalities allows for spatial correlations of elements and their local molecular environments to be performed, further enhancing our knowledge of disease status and progression. A better understanding of pathogenesis at this level will enable the development of more efficient treatments [8–12].

Elemental analysis can reveal elemental dysregulation, accumulation or depletion, which are well described for many diseases such as Alzheimer’s disease [13], tuberculosis [14] and cancer [15–17]. Alkali metals in particular have been the subject of extensive research and are implicated in various neurodegenerative and infectious diseases as they are also known to disrupt lipid metabolism and play a key role in cell homeostasis [16–19]. Understanding the collocation of alkali metals with host biomolecules such as lipids and

metabolites at the tissue level may shed new light on disease pathogenesis. Alkali metals and other trace elements can be imaged using elemental mapping techniques [7,20–22] such as laser ablation inductively couple mass spectrometry (LA-ICP-MS) [23–29], X-ray fluorescence (XRF) [30–35] and particle-induced X-ray emission (PIXE) [36–41], which have been extensively applied to the analysis of biological samples.

There are a multitude of mass spectrometry imaging (MSI) techniques available [42–44] for imaging biological samples, including the commercially available desorption electrospray ionisation (DESI) [45–49], matrix-assisted laser desorption ionisation (MALDI) [50–53] and secondary ion mass spectrometry (SIMS) [54–58]. These techniques can provide images of the distribution of lipids, metabolites and (to a lesser extent) proteins [59,60]. Whilst these are primarily molecular analysis techniques, some reports in the literature have described how a limited amount of elemental information can be extracted using these techniques. SIMS can readily offer both molecular and elemental information, although the level of molecular information is highly dependent on the primary ion [58]. Additionally, the matrix effects preclude quantitative analysis [61,62]. MALDI is primarily used for molecular mapping, but Liu et al. reported on a workflow to target lipids, small metabolites and alkali ions (sodium and potassium) using this technique [63]. Most recently, a variant of DESI—nanoDESI—was used to simultaneously monitor metal ions (sodium and potassium) and metabolites [19]. Despite the seeming ability of these techniques to target both elements and molecules, the range of elements readily detectable and the quantitative capabilities are limited when compared to the primary elemental techniques listed above.

In most previous studies, sequential MSI and elemental mapping were performed on sequential tissue sections. A limitation of this approach is that smaller features are not accurately replicated in sequential sections, reducing the accuracy of feature collocation. It is therefore desirable to perform the two measurements sequentially using the same tissue sample. This is not trivial due to sample preparation incompatibility and modifications incurred to the samples by the preceding analysis. For example, it is reasonable to expect that elemental mapping using any of the techniques described above would modify the chemistry of the sample due to localised heating, and indeed this has been previously demonstrated in the case of PIXE [64,65]. It is therefore desirable to develop molecular imaging strategies that do not delocalise elemental species. In previous work, it was shown that DESI imaging, employing a MeOH:H₂O electrospray solvent, preserved the location and concentration of various elemental species in lung tissues, for example Fe and S. However, elements such as Cl and K were delocalised by the DESI analysis and could not be imaged.

DESI offers the prospect of analysis under ambient conditions, meaning that the sample is analysed in its native state. It offers further advantages in terms of analyte coverage for lipids and metabolites [66]. Here we report on a novel DESI electrospray solvent system (MeOH:EtOH), which enables subsequent elemental mapping using the same tissue section without the delocalisation of Cl and K and other detected trace elements. This solvent combination was previously used by Lewis et al., who used direct analyte probed nanoextraction (DAPNe) for the extraction and analysis of lipids from tissue sections with no detrimental effect on the subsequent elemental imaging, but to our knowledge, this has not been used before with DESI [67].

The ion beam analysis (IBA) techniques PIXE and Elastic Backscattering Spectrometry (EBS) were used to monitor the delocalisation and loss of elements following DESI imaging. To assess the performance of the MeOH:EtOH solvent system to image the molecular species, a benchmarking experiment was performed to compare the new MeOH:EtOH to the widely used MeOH:H₂O solvent system [64,65]. This was carried out by comparing the intensities and coverage of the lipid peaks observed in homogenised liver. The analytical workflow was then applied to a lung tissue section containing a tuberculosis lesion, enabling an integrated analysis of alkali ions, transition metals, halogens and lipids.

2. Materials and Methods

2.1. Sample Preparation

2.1.1. Homogenized Tissue

Rat liver homogenates were prepared as described by Swales et al. [68] The liver tissue was homogenised and pipetted into moulds (2 mL bottom end of Pasteur pipette bulb). The homogenates were snap frozen in propanol and then iso-pentane and were stored in $-80\text{ }^{\circ}\text{C}$. Three homogenates were sectioned sequentially at $10\text{ }\mu\text{m}$ thickness using a Thermo NX70 Cryostar (Thermo Fisher Scientific, Bremen, Germany) and were thaw mounted onto a $1.4\text{ }\mu\text{m}$ thick polyethylene (PET) substrate (Leica, Wetzlar, Germany). The slides were analysed sequentially using DESI and PIXE/EBS in the areas highlighted in Figure S1. All animals and tissue were managed in accordance with the UK Home Office Animals (Scientific Procedures) Act 1986. The organs used within this study were within the 3Rs principles as they comprised a control material surplus to the original study for which they were intended.

2.1.2. Snap-Frozen Lung Tissue

Rabbit infection and sample collection were performed in Biosafety Level 3 (BSL3) facilities and approved by the Institutional Animal Care and Use Committee of the National Institute of Allergy and Infection Disease, NIH, Bethesda, MD, USA (Protocol number LCIM-3). All studies followed the guidelines and basic principles stated in the United States Public Health Service Policy on Humane Care and Use of Laboratory Animals. All samples collected from *Mycobacterium tuberculosis*-infected animals were handled and processed in the BSL3 in compliance with protocols approved by the Institutional Biosafety Committee of the National Institute of Allergy and Infection Disease, NIH, and Hackensack Meridian Health, NJ, USA.

Female New Zealand White (NZW) rabbits weighing 2.2–2.6 kg were maintained under specific pathogen-free conditions and fed water and chow ad libitum. The NZW rabbit ID 713 was infected with *M. tuberculosis* HN878 using a nose-only aerosol exposure system as described [69]. At 14 weeks postinfection, once mature cellular and necrotic lung lesions had developed, lung lesions embedded in the surrounding tissue were collected for imaging and were snap frozen (unprocessed) in liquid nitrogen vapor as described previously [70,71]. To sterilize the samples and inactivate all viable *M. tuberculosis* bacilli, samples were γ -irradiated in a Co-60 irradiator until exposure reached 3 Mrad (validated as a sufficient exposure to kill all viable *M. tuberculosis* bacteria present in lung lesions). Dry ice was resupplied as required to keep the samples always frozen. The frozen rabbit lesions were sectioned at a $10\text{ }\mu\text{m}$ thickness using a CM1860 UV cryostat (Leica, Wetzlar, Germany) at $-20\text{ }^{\circ}\text{C}$. The sections were thaw mounted onto $1.4\text{ }\mu\text{m}$ thick poly(ethylene terephthalate) (PET) membrane slides (Leica, Wetzlar, Germany), shipped on dry ice and stored at $-80\text{ }^{\circ}\text{C}$.

2.2. DESI Imaging

DESI was used to image small molecules in the tissue homogenates prior to the ion beam analysis. A prototype DESI source with a recessed capillary (Waters, Wilmslow, UK) was coupled to a Xevo G2-XS (Waters, Wilmslow, UK) mass spectrometer. A 95:5 (%v/v) methanol (MeOH)/water (H_2O) or 50:50 (%v/v) MeOH/ethanol (EtOH) spray solvent was delivered at a rate of $2\text{ }\mu\text{L}/\text{min}$ using an Ultimate 3000 UHPLC system (Thermo Fisher Scientific, Bremen, Germany) with an electrospray voltage of 0.6 kV and ion block temperature set to $100\text{ }^{\circ}\text{C}$. Prior to acquisition, mass calibration in positive ion mode was performed using a polylactic acid (PLA) sublimed slide made in house with a collision energy of 35 V. Data were acquired in positive ion “sensitivity” mode, with a mass range of m/z 100–1200 at a calculated mass resolving power of 15,000 at m/z 200. The tissue region for imaging was selected using High-Definition Imaging (Waters, Wilmslow, UK) software. The nominal pixel size was $75 \times 75\text{ }\mu\text{m}$ using a stage speed of $150\text{ }\mu\text{m}/\text{s}$, acquiring the data at 2 pixels/s.

Data Analysis—DESI

Waters RAW data files were converted into imzML files through a two-step conversion. The first was the conversion to mzML using Proteowizard [72], then to an imzML using the imzML converter [73]. The imzML data were analysed using Spectral Analysis [74] (version 1.4.0) and run using MATLAB (version 2018b). Prior to generating a mean spectrum, the data were preprocessed using a rebinning method (bin size of 0.001) to generate the mean spectra, and then they were normalised to the total ion intensity when generating the datacube.

A lipid peak list (top 50 most intense peaks assigned as lipids) was generated through the tentative assignment of m/z peaks detected in the liver homogenates (see Table S2) using in-house MATLAB scripts which matched the data against the Human Metabolome Database (HMDB) [75]. The peak assignment was achieved using a ± 15 ppm mass match and through the inspection of the DESI ion images to ensure that the signals originated from the sample and not the background. Peak assignments were further checked against criteria such as abundance in mammalian tissue, likelihood of adduct formation and likelihood of ion formation in positive ion mode.

2.3. Ion Beam Analysis

After DESI, the samples were simultaneously analysed by proton induced X-ray emission (PIXE) and elastic backscattered spectrometry (EBS) using a 2 MV Tandem accelerator (High Voltage Engineering, Amersfoort, The Netherlands). The samples were placed in a vacuum chamber pumped to 10^{-6} mBar and irradiated using 2.5 MeV protons with beam currents ranging from 300–600 pA. The beam was focused to approximately $2 \times 2 \mu\text{m}$ (measured using a $75 \times 75 \mu\text{m}$ 1000 copper grid). The scan size was $1 \times 1 \text{ mm}$ with a pixel dwell time set at 0.3 ms. X-rays were detected using a silicon drift detector (SDD) fitted with a $130 \mu\text{m}$ Be filter, mounted at an angle of 135° to the beam direction in the horizontal plane. Backscattered particles were simultaneously collected and detected using a PIPS detector with an active area of 150 mm^2 , placed 52.5 mm away from the sample and mounted at a 25° exit angle.

The liver homogenate samples were analysed until a charge of 2000 nC was collected in the areas highlighted in Figure S1. Three sequential rabbit lesion sections were analysed in mosaic scan mode (2×2 squares of $1 \times 1 \text{ mm}$ each), with each square being analysed until 4000 nC of charge were collected.

Data Analysis—Ion Beam Analysis

The X-ray and backscattered particle spectra were calibrated using a BCR-126A lead glass standard. The data were acquired and analysed using OMDAQ-3 software (Oxford Microbeams, Ltd., Oxfordshire, UK) [76].

3. Results

3.1. Homogenized Tissue

As highlighted in Figure S1, selected regions of three sequential liver homogenate sections were analysed by DESI using two different solvent systems: 95:5 (%v/v) MeOH/H₂O or 50:50 (%v/v) MeOH/EtOH. Each section was then imaged by PIXE/EBS with an ROI encompassing the interface of the areas sampled by DESI to observe delocalisation.

A sequential PIXE analysis at the interface of the areas previously analysed by DESI clearly demonstrated that the MeOH:H₂O solvent caused a visible loss of mobile ions such as chlorine and potassium as well as phosphorus, as shown in Figure 1A. Conversely, the MeOH:EtOH solvent caused no measurable loss or delocalisation of any elements measured by PIXE (Figure 1B). This was further supported by Figure S2, showing the overlay of the PIXE spectra taken from regions of interest derived from areas with/without prior DESI analysis, and by Figure 1C, which shows the signal loss for several elements after DESI analysis. Statistical tests (t -tests) showed that the differences observed in the PIXE peak

area ratios measured between the two solvents were statistically significant for all elements monitored (see Table S1).

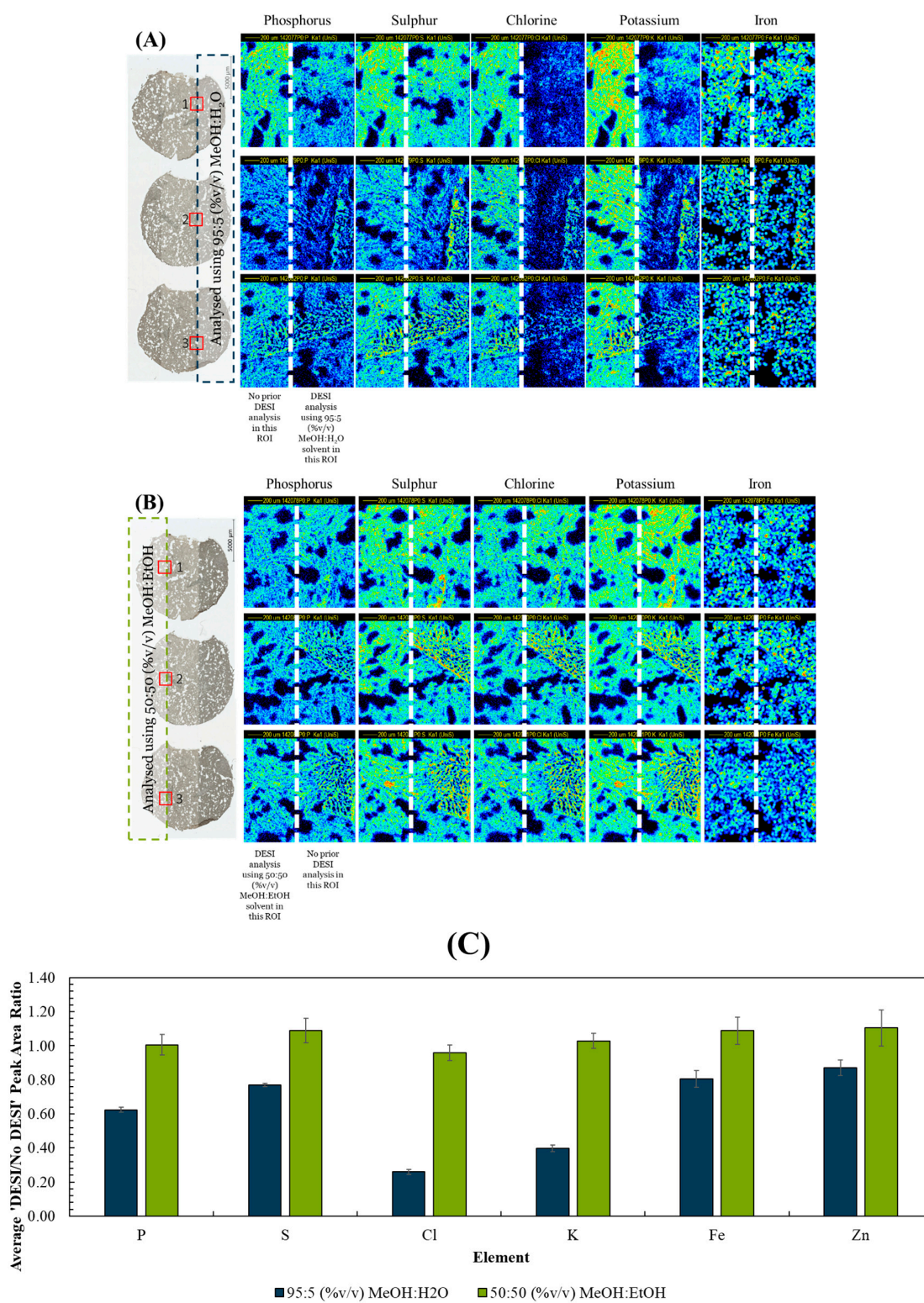


Figure 1. PIXE maps taken post-DESI from 3 sequential liver homogenate sections using an ROI scanned over the edge of the DESI ROI using (A) 95:5 (%v/v) MeOH:H₂O and (B) 50:50 (%v/v) MeOH:EtOH. The DESI (dotted line) and PIXE ROIs (solid line) are indicated on the far-left image. (C) Average ratio ($n = 3$) of the elemental peak areas measured by PIXE from ROIs with/without prior DESI. See Figure S1 for further information on the analysis locations for each technique.

Figure S3 shows example DESI spectra taken with each solvent system from the background (PET substrate) and shows that the MeOH/EtOH mixture generated less intense peaks from the PET background. Figure 2 compares the mean spectra collected from tissue ROIs corresponding to analysis via the two solvent mixtures. The spectra were broadly similar, with the 50:50 (%v/v) MeOH:EtOH solvent producing slightly higher TIC-normalised peak intensities than MeOH:H₂O, especially in the higher m/z ranges, possibly due to the higher solubility of lipids in the purely organic solvent.

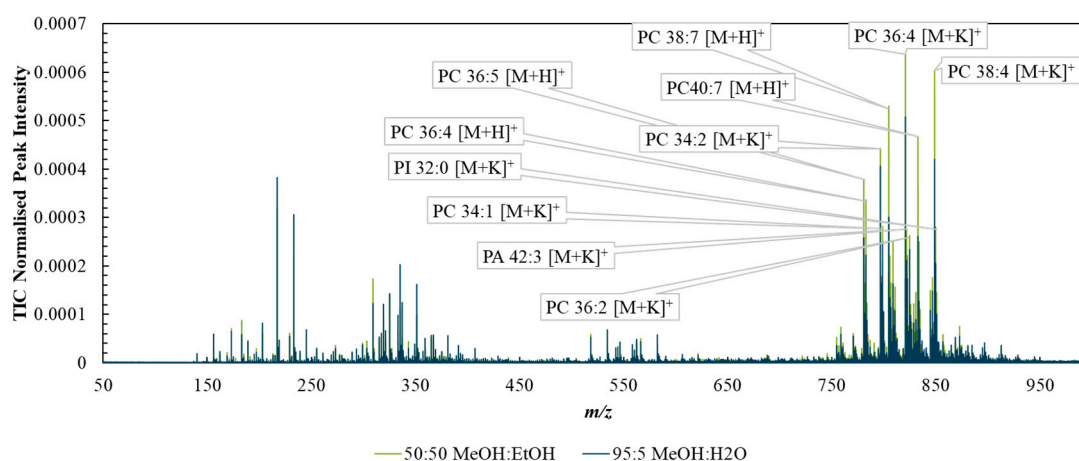


Figure 2. Spectra taken from regions of interest capturing tissue-only areas acquired with DESI using the two solvent systems—95:5 (%v/v) methanol/water (blue) or 50:50 (%v/v) methanol/ethanol (green).

The top 50 most intense lipid peaks were selected, and a list of measured m/z and peak assignments are listed in Table S2. The breakdown per assigned lipid class (Figure 3A) and per m/z range (Figure S4) were compared for each spray solvent. The intensities of the 10 most intense peaks for each solvent were compared in Figure 3B,C. As expected, these were comprised predominantly of peaks assigned to phosphocholines (PC), due to their prevalence in cell membranes. The two datasets shared 9 out of the 10 lipid peaks (marked by the asterisks) and these were detected with statistically significant higher peak intensities ($p < 0.05$; see Table S3) when the MeOH:EtOH solvent was used. Ion images were generated for each of the 10 peaks, and all were shown to originate from the tissue homogenate rather than the background (Figure S5). Figure S6 shows the peak intensity measured for the remaining 40 top lipid peaks for each solvent. These observations, as well as Figure 3, demonstrate that the two solvents did not preferentially target lipids in one particular m/z region of the mass spectrum.

A brief study of the adducts formed using the two solvent systems showed that MeOH:EtOH produced more $[M+K]^+$ adducts in the top 50 lipids than MeOH:H₂O (see Figure S7). This is interesting as the PIXE data showed that MeOH:EtOH did not cause a loss or delocalization of potassium, offering a possible explanation for the increased proportion of intense lipid peaks appearing as $[M+K]^+$. In contrast, the ratio $[M+H]^+ / [M+K]^+$ for a selection of PC lipids was found not to change significantly between the two solvent systems (see Figure S7). Future work could explore whether the addition (and preservation) of K in biological samples can be used to enhance lipid coverage.

The data shown above demonstrate that using 50:50 (%v/v) MeOH:EtOH as a DESI electrospray solvent can be advantageous for increasing the sensitivity to lipids. Additionally, the data showed that the new solvent did not cause the removal or delocalisation of mobile ions as measured by PIXE. To confirm this observation, and to demonstrate the ability of MeOH:EtOH to provide images, these two solvent systems were used to analyse the snap-frozen lung tissue sections.

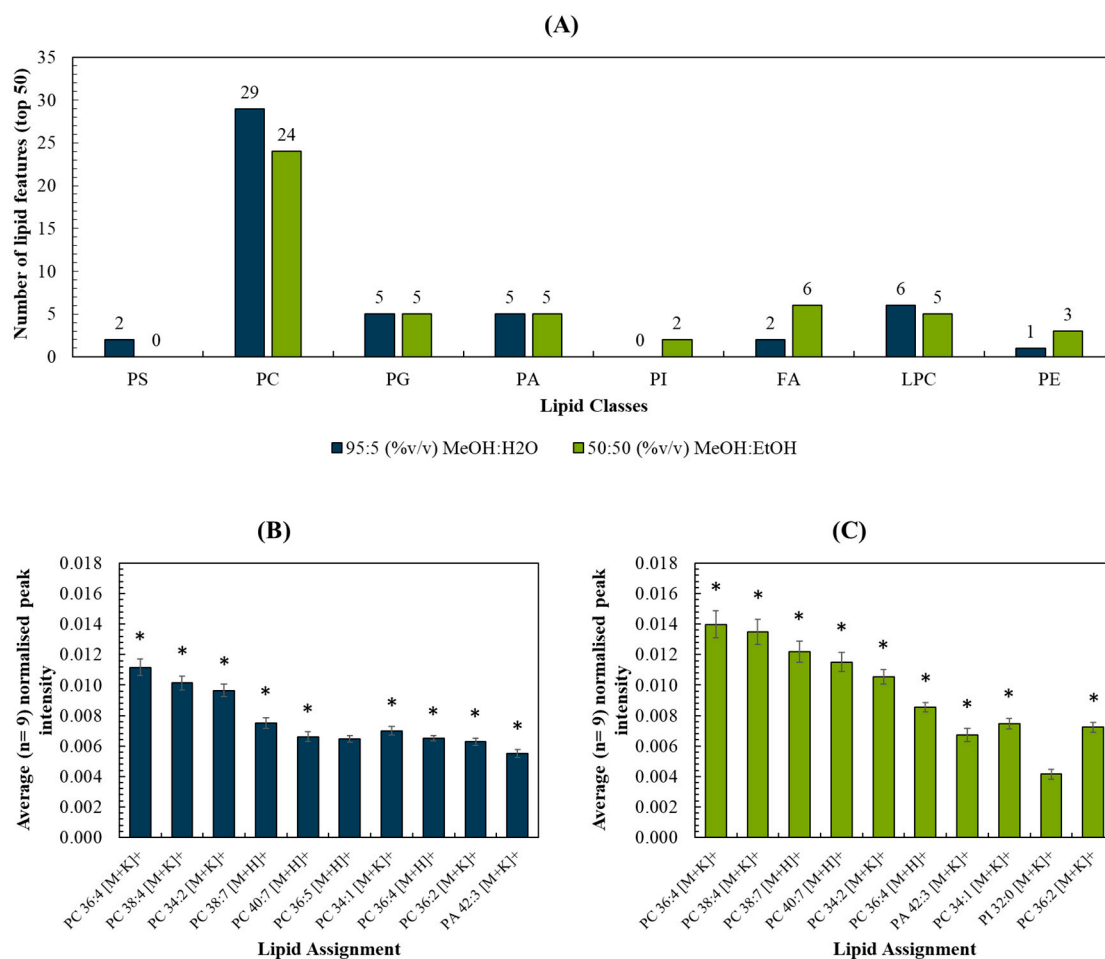


Figure 3. (A) Number of lipid features (out of the top 50) detected per lipid classes for MeOH:H₂O and MeOH:EtOH spray solvents, respectively; (B,C) Top 10 most abundant peaks and their respective intensities (normalised to the total ion count) for (B) MeOH:H₂O and (C) MeOH:EtOH. * refers to peaks detected using both solvents in liver homogenates.

3.2. Snap-Frozen Lung Tissue from Rabbits

The optical images taken before the DESI analysis of the of snap-frozen rabbit lung tissues containing a caseous granuloma (a lesion caused by tuberculosis) is shown in Figure S8. Two of the sections were first analysed using the two DESI solvents and a third were left untouched to be used as a control for ion beam elemental mapping. The regions were chosen to include three regions of the granuloma—the caseum or necrotic centre, cellular rim and uninvolved lung.

Figure 4 shows the red, green and blue (RGB) overlay of m/z 953 (TG (58:8) $[M+Na]^+$), m/z 832 (PC (38:4) $[M+K]^+$) and m/z 780 (PC(36:5) $[M+H]^+$) obtained using DESI and two spray solvents—95:5 (%v/v) MeOH:H₂O and 50:50 (%v/v) MeOH:EtOH. These peaks were chosen because they very clearly show the different pathology regions of the granuloma tissue. In both overlays, the different regions of the granulomas were visible, as presented in Figure S8. Figure 4 demonstrates that the MeOH:EtOH spray solvent could produce images of comparable quality to the more widely used MeOH:H₂O.

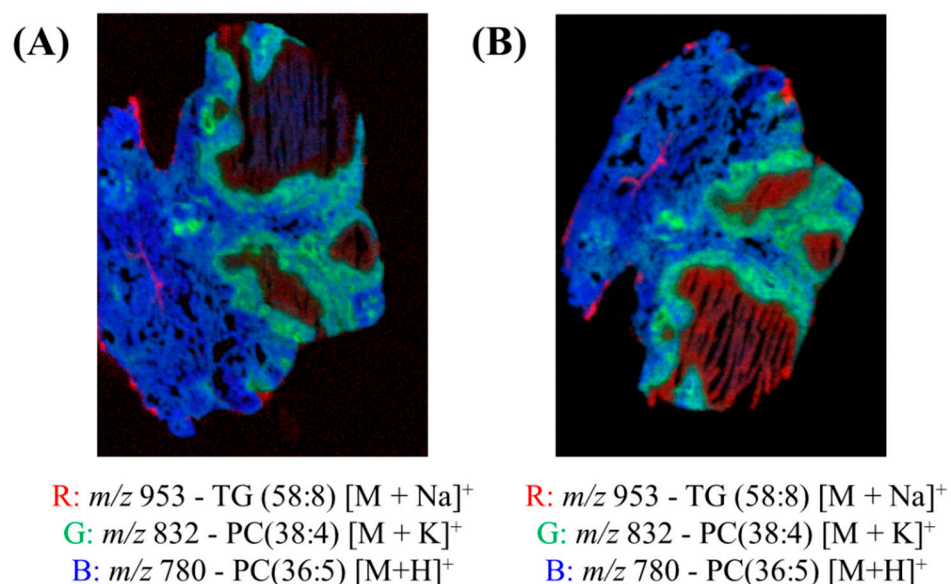


Figure 4. Red, green and blue (RGB) overlay of m/z 953 (TG (58:8) $[M+Na]^+$), m/z 832 (PC (38:4) $[M+K]^+$) and m/z 780 (PC(36:5) $[M+H]^+$) obtained using DESI and two spray solvents—(A) 95:5 (%v/v) MeOH:H₂O and (B) 50:50 (%v/v) MeOH:EtOH.

The chlorine (Cl) and potassium (K) elemental maps from a sequential PIXE analysis of the three tissue sections are shown in Figure 5. As shown in the maps in Figure 5, there was a loss of Cl and K when MeOH:H₂O was used as a spray solvent ($p > 0.05$; see Table S4), but Fe remained unchanged. Figure S9 shows the remaining elemental maps for phosphorus (P), sulphur (S) and the total EBS map.

As each of the lung sections were analysed in mosaic scan mode (four squares arranged in a 2×2 array, each square of dimensions 1×1 mm), there were four analysis regions per sample. Figure S10 shows the overlay of the X-ray spectra for one of the squares—the one in each sample which captured the caseum. There is a clear loss of K and Cl when MeOH:H₂O was used, in agreement with the elemental maps shown in Figure 5. As observed with the tissue homogenate sections, there was a small loss of P when the MeOH:H₂O solvent was used, confirmed by t -test ($p < 0.05$, see Table S4). On the other hand, the difference in P peak area between the control sample and the sample analysed using MeOH:EtOH was not statistically different ($p > 0.05$). This confirmed that MeOH:EtOH could preserve the elemental integrity of the sample.

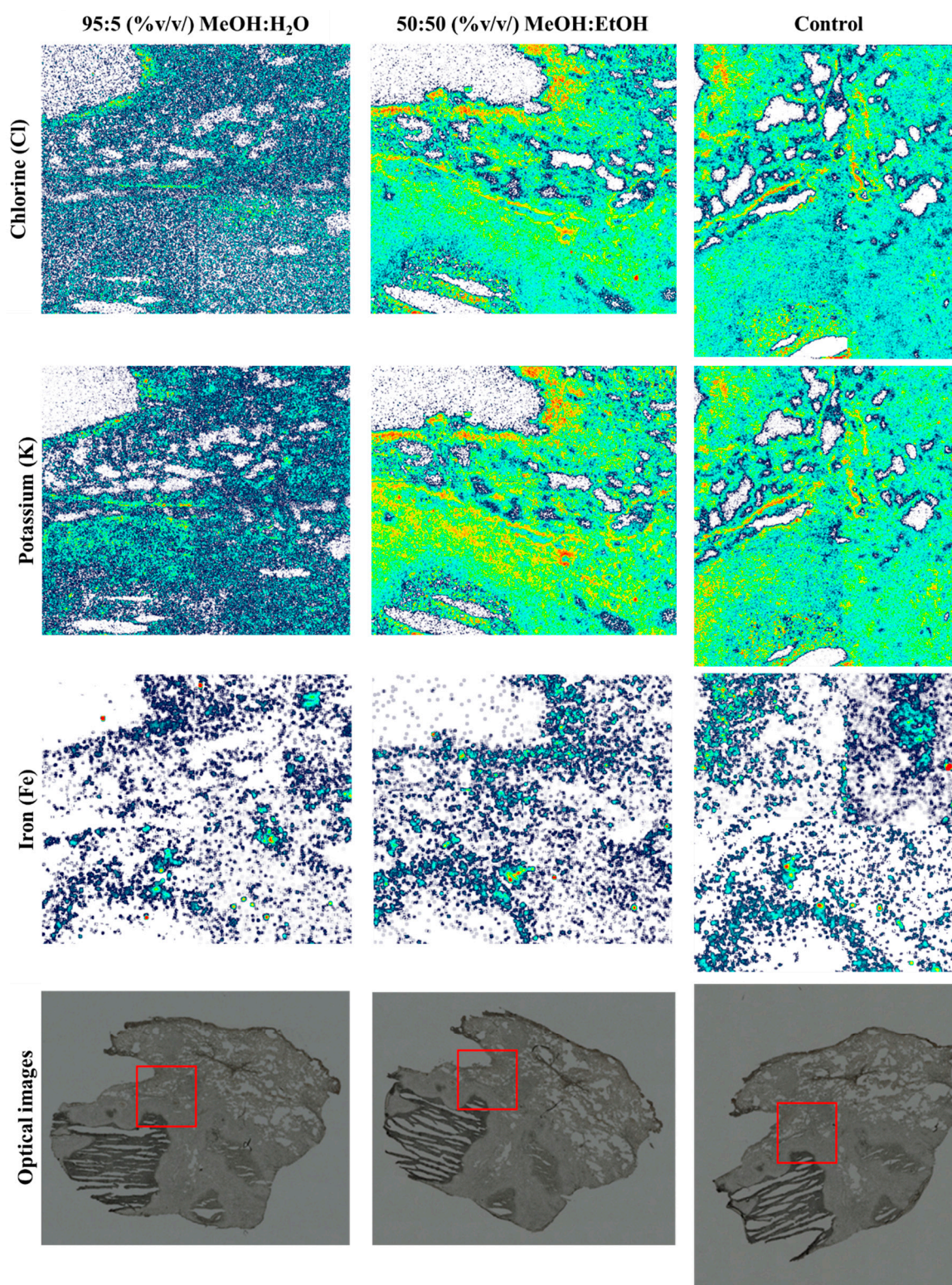


Figure 5. Chlorine (Cl), potassium (K) and iron (Fe) PIXE maps taken from snap-frozen lung tissue sections after DESI analysis using 95:5 (%v/v) MeOH:H₂O or 50:50 (%v/v) MeOH:EtOH. A third section (control) was also analysed—no DESI measurements were taken on this sample. Optical images taken before analysis highlighting the PIXE/EBS analysis areas (red squares) on each tissue.

4. Discussion

The data presented here demonstrates that elemental mapping can be carried out following DESI imaging using a 50:50 (%v/v) MeOH:EtOH spray solvent. To our knowl-

edge, this is the first time that this solvent system has been reported for use in a DESI system, although it is noteworthy that MeOH:EtOH has been used previously by Lewis et al. for liquid extraction surface analysis to enable the extraction of lipids from tissue sections [67]. Our data showed that this novel solvent system can produce images of similar quality (Figure 4) to the more conventional MeOH:H₂O solvent system, with similar coverage across the mass spectrum (Figure S6) and enhanced an signal-to-noise ratio for selected peaks (Figure 3). The increased sensitivity towards lipids using this alcohol-based spray solvent may be related to the known effect of alcohols on lipid bilayer properties. Alcohols, and in particular ethanol and methanol, are known to change the structural properties of membranes, increasing their permeability. In this instance, it is expected that the employment of these solvents for DESI analysis would increase the sensitivity towards lipids [77]. Furthermore, no delocalisation or loss of elements was observed using PIXE/EBS. This is presumably because mobile ions such as potassium and chlorine are highly water soluble and so delocalise in the conventional MeOH:H₂O solvent system, but not in the aqueous-free novel solvent mixture.

We have therefore demonstrated the successful multimodal imaging of molecular and elemental markers on a single tissue section, overcoming issues such as changes incurred to the samples by preceding measurements. In this work we have shown that IBA can be carried out following DESI analysis, but this observation is also relevant to other elemental imaging techniques such as XRF, SEM and LA-ICP-MS, for example.

A limitation of the current approach is that the image resolution of commercial DESI instrumentation (typically 50–100 microns) is inferior to many elemental imaging modalities, which can be submicron, depending on the technique. Elemental mapping techniques can resolve single cells, whereas most DESI systems currently cannot. Being able to resolve single cells would improve the certainty of correlation between molecular and elemental images. Recent developments in DESI source technology should drive substantial improvements to image resolution and enable imaging at comparable pixel sizes in the near future [78].

Future work should investigate different ratios of methanol to ethanol and whether this changes the sensitivity/coverage of the DESI analysis and/or the elemental composition of a sample. Additionally, it would be useful to use PIXE to establish whether the absence of potassium caused by the MeOH:H₂O solvent prevents [M+K]⁺ adduct formation, thereby reducing sensitivity to certain lipids. The preservation (or even addition) of K in biological samples may be useful to enhance lipid coverage.

5. Conclusions

This work has demonstrated that the novel DESI spray solvent 50:50 (%v/v) methanol:ethanol enables sequential elemental mapping out on the same tissue section. This is desirable to allow the accurate correlation of elemental and molecular features since regions of interest are not always accurately reproduced in sequential sections. In this work, the new solvent system produced similar, if not better, lipid coverage and sensitivity in positive ion mode when compared to the conventional methanol:water solvent. This work therefore demonstrates the successful multimodal imaging of molecular and elemental markers on a single tissue section, overcoming issues such as changes incurred to the samples by preceding measurements.

Supplementary Materials: The following supporting information can be downloaded at <https://www.mdpi.com/article/10.3390/metabo13020262/s1>: Figure S1: Additional analysis information; Figure S2: X-ray spectra overlay of areas analysed with DESI on areas not analysed with DESI; Table S1: T-tests results for elemental concentrations measured from liver homogenates; Figure S3: Overlay of DESI spectra taken from the background using the two different solvents; Table S2: Top 50 lipid features detected in the liver homogenates; Figure S4: Histogram showing the top 50 lipid distribution per *m/z* range; Table S3: T-test results for the top 10 lipids detected using both solvents; Figure S5: DESI maps obtained from liver homogenates using the two solvents; Figure S6: Peak intensities for the remaining top 40 lipid features detected in liver homogenates using DESI; Figure S7: Optical

and H&E images of snap-frozen rabbit lung; Table S4: T-test results for elemental concentrations measured with PIXE rabbit lung section; Figure S8: PIXE maps for P, S and EBS map taken from the rabbit lung section; Figure S9: Overlay of X-ray spectra taken after DESI imaging using each solvent.

Author Contributions: Conceptualisation, C.C. and M.J.B.; methodology, C.C., M.J.B., V.P. and G.W.G.; software, T.M. and G.W.G.; formal analysis, C.C., J.D.J. and C.N.; resources, J.D.J., C.N., K.F., V.D., R.W., J.B. and M.J.B.; data curation, C.C.; writing—original draft preparation, C.C. and M.J.B.; review and editing, all authors; supervision, M.J.B.; funding acquisition, M.J.B. and R.W. All authors have read and agreed to the published version of the manuscript.

Funding: This work was supported by an EPSRC-funded fellowship EP/R031118/1. We also acknowledge the funding from the NPL-Surrey iCASE studentship award, Dr. M. Al-Sid-Cheikh's Fellowship from the Analytical Chemistry Trust Fund (grant number: 600310/10) and the Capital award from NERC: the Applied-Radioisotope & Environmental Laboratory (ARIEL) (grant number: NE/V017616/1) for the cryostat used in this research. The beam time was provided by the EPSRC National Research Facility UKNIBC NS/A000059/1 and RADIATE (Horizon 2020, grant agreement No 824096, proposal 19001813-ST). The authors thank Laura E Via and Danielle Weiner from the NIAID-NIH for providing the infected lung tissues.

Institutional Review Board Statement: For the liver homogenates, all animals and tissue were managed in accordance with the UK Home Office Animals (Scientific Procedures) Act 1986. The organs used within this study were within the 3Rs principles as they comprised control material surplus to the original study for which they were intended. Rabbit infection and sample collection were performed in Biosafety Level 3 (BSL3) facilities and approved by the Institutional Animal Care and Use Committee of the National Institute of Allergy and Infection Disease, NIH, Bethesda, MD (Protocol number LCIM-3). All studies followed the guidelines and basic principles stated in the United States Public Health Service Policy on Humane Care and Use of Laboratory Animals.

Informed Consent Statement: Not applicable.

Data Availability Statement: All datasets generated for this study are included in the article.

Acknowledgments: Graphical abstract licensed to Kyle Saunders using BioRender.com.

Conflicts of Interest: The authors declare no conflict of interest.

References

1. Walter, A.; Paul-Gilloteaux, P.; Plochberger, B.; Sefc, L.; Verkade, P.; Mannheim, J.G.; Slezak, P.; Unterhuber, A.; Marchetti-Deschmann, M.; Ogris, M.; et al. Correlated Multimodal Imaging in Life Sciences: Expanding the Biomedical Horizon. *Front. Phys.* **2020**, *8*, 47. [[CrossRef](#)]
2. Matusch, A.; Fenn, L.S.; Depboylu, C.; Klietz, M.; Strohmer, S.; McLean, J.A.; Becker, J.S. Combined Elemental and Biomolecular Mass Spectrometry Imaging for Probing the Inventory of Tissue at a Micrometer Scale. *Anal. Chem.* **2012**, *84*, 3170–3178. [[CrossRef](#)]
3. Svirikova, A.; Turyanskaya, A.; Perneckzy, L.; Strel, C.; Marchetti-Deschmann, M. Multimodal imaging of undecalcified tissue sections by MALDI MS and μ XRF. *Analyst.* **2018**, *143*, 2587–2595. [[CrossRef](#)] [[PubMed](#)]
4. Touboul, D.; Roy, S.; Germain, D.P.; Chaminade, P.; Brunelle, A.; Lapr votte, O. MALDI-TOF and cluster-TOF-SIMS imaging of Fabry disease biomarkers. *Int. J. Mass. Spectrom.* **2007**, *260*, 158–165. [[CrossRef](#)]
5. Flint, L.E.; Hamm, G.; Ready, J.D.; Ling, S.; Duckett, C.J.; Cross, N.A.; Cole, L.M.; Smith, D.P.; Goodwin, R.J.A.; Clench, M.R. Characterization of an Aggregated Three-Dimensional Cell Culture Model by Multimodal Mass Spectrometry Imaging. *Anal. Chem.* **2020**, *92*, 12538–12547. [[CrossRef](#)]
6. Petibois, C. Imaging methods for elemental, chemical, molecular, and morphological analyses of single cells. *Anal. Bioanal. Chem.* **2010**, *397*, 2051–2065. [[CrossRef](#)]
7. Perry, W.J.; Weiss, A.; Van de Plas, R.; Spraggins, J.M.; Caprioli, R.M.; Skaar, E.P. Integrated molecular imaging technologies for investigation of metals in biological systems: A brief review. *Curr. Opin. Chem. Biol.* **2020**, *55*, 127–135. [[CrossRef](#)] [[PubMed](#)]
8. Szpunar, J. Advances in analytical methodology for bioinorganic speciation analysis: Metallomics, metalloproteomics and heteroatom-tagged proteomics and metabolomics. *Analyst.* **2005**, *130*, 442–465. [[CrossRef](#)] [[PubMed](#)]
9. Naga Raju, G.J.; John Charles, M.; Bhuloka Reddy, S.; Sarita, P.; Seetharami Reddy, B.; Rama Lakshmi, P.V.B.; Vijayan, V. Trace elemental analysis in cancer-afflicted tissues of penis and testis by PIXE technique. *Nucl. Instrum. Methods Phys. Res. B.* **2005**, *229*, 457–464. [[CrossRef](#)]
10. Rajendran, R.; Minqin, R.; Ronald, J.A.; Rutt, B.K.; Halliwell, B.; Watt, F. Does iron inhibit calcification during atherosclerosis? *Free Radic. Biol. Med.* **2012**, *53*, 1675–1679. [[CrossRef](#)]
11. Ren, M.Q.; Ji, X.; Vajandar, S.K.; Mi, Z.H.; Hoi, A.; Walczyk, T.; van Kan, J.A.; Bettiol, A.A.; Watt, F.; Osipowicz, T. Analytical possibilities of highly focused ion beams in biomedical field. *Nucl. Instrum. Methods Phys. Res. B.* **2017**, *406*, 15–24. [[CrossRef](#)]

12. Jeynes, C.; Bailey, M.J.; Coley, H.; Kirkby, K.J.; Jeynes, C. Microbeam PIXE analysis of platinum resistant and sensitive ovarian cancer cells. *Nucl. Instrum. Methods Phys. Res. B* **2010**, *268*, 2168–2171. [[CrossRef](#)]
13. Murray, F.E.S.; Landsberg, J.P.; Williams, R.J.P.; Esiri, M.M.; Watt, F. Elemental Analysis of Neurofibrillary Tangles in Alzheimer's Disease Using Proton-Induced X-ray Analysis. In *Ciba Foundation Symposium 169-Aluminium in Biology and Medicine: Aluminium in Biology and Medicine: Ciba Foundation Symposium 169*; John Wiley & Sons, Ltd.: Chichester, UK, 28 September 2007; pp. 201–216.
14. Basaraba, R.J.; Bielefeldt-Ohmann, H.; Eschelbach, E.K.; Reisenhauer, C.; Tolnay, A.E.; Taraba, L.C.; Shanley, C.A.; Smith, E.A.; Bedwell, C.L.; Chlipala, E.A.; et al. Increased expression of host iron-binding proteins precedes iron accumulation and calcification of primary lung lesions in experimental tuberculosis in the guinea pig. *Tuberculosis* **2008**, *88*, 69–79. [[CrossRef](#)] [[PubMed](#)]
15. González de Vega, R.; Fernández-Sánchez, M.L.; Pisonero, J.; Eiró, N.; Vizoso, F.J.; Sanz-Medel, A. Quantitative bioimaging of Ca, Fe, Cu and Zn in breast cancer tissues by LA-ICP-MS. *J. Anal. At. Spectrom.* **2017**, *32*, 671–677. [[CrossRef](#)]
16. Ramos, P.; Santos, A.; Pinto, E.; Pinto, N.R.; Mendes, R.; Magalhães, T.; Almeida, A. Alkali metals levels in the human brain tissue: Anatomical region differences and age-related changes. *J. Trace Elem. Med. Biol.* **2016**, *38*, 174–182. [[CrossRef](#)]
17. Salina, E.G.; Waddell, S.J.; Hoffmann, N.; Rosenkrands, I.; Butcher, P.D.; Kaprelyants, A.S. Potassium availability triggers Mycobacterium tuberculosis transition to, and resuscitation from, non-culturable (dormant) states. *Open Biol.* **2014**, *4*. [[CrossRef](#)] [[PubMed](#)]
18. Kato, S.; Shimizu, N.; Ogura, Y.; Otoki, Y.; Ito, J.; Sakaino, M.; Sano, T.; Kuwahara, S.; Takekoshi, S.; Imagi, J.; et al. Structural Analysis of Lipid Hydroperoxides Using Mass Spectrometry with Alkali Metals. *J. Am. Soc. Mass Spectrom.* **2021**, *32*, 2399–2409. [[CrossRef](#)] [[PubMed](#)]
19. Mavrouidakis, L.; Duncan, K.D.; Lanekoff, I. Host-Guest Chemistry for Simultaneous Imaging of Endogenous Alkali Metals and Metabolites with Mass Spectrometry. *Anal. Chem.* **2022**, *94*, 2391–2398. [[CrossRef](#)]
20. da Cunha, M.M.L.; Trepout, S.; Messaoudi, C.; Wu, T.-D.; Ortega, R.; Guerin-Kern, J.-L.; Marco, S. Overview of chemical imaging methods to address biological questions. *Micron.* **2016**, *84*, 23–36. [[CrossRef](#)] [[PubMed](#)]
21. Wu, B.; Becker, J.S. Imaging techniques for elements and element species in plant science. *Metallomics.* **2012**, *4*, 403–416. [[CrossRef](#)]
22. Jeynes, C.; Colaun, J.L. Thin film depth profiling by ion beam analysis. *Analyst* **2016**, *141*, 5944–5985. [[CrossRef](#)]
23. Bonta, M.; Gonzalez, J.J.; Quarles, C.D.; Russo, R.E.; Hegedus, B.; Limbeck, A. Elemental mapping of biological samples by the combined use of LIBS and LA-ICP-MS. *J. Anal. At. Spectrom.* **2016**, *31*, 252–258. [[CrossRef](#)]
24. Martinez, M.; Baudalet, M. Calibration strategies for elemental analysis of biological samples by LA-ICP-MS and LIBS – A review. *Anal. Bioanal. Chem.* **2020**, *412*, 27–36. [[CrossRef](#)] [[PubMed](#)]
25. Pozebon, D.; Scheffler, G.L.; Dressler, V.L. Recent applications of laser ablation inductively coupled plasma mass spectrometry (LA-ICP-MS) for biological sample analysis: A follow-up review. *J. Anal. At. Spectrom.* **2017**, *32*, 890–919. [[CrossRef](#)]
26. Pozebon, D.; Scheffler, G.L.; Dressler, V.L.; Nunes, M.A.G. Review of the applications of laser ablation inductively coupled plasma mass spectrometry (LA-ICP-MS) to the analysis of biological samples. *J. Anal. At. Spectrom.* **2014**, *29*, 2204–2228. [[CrossRef](#)]
27. Sussulini, A.; Becker, J.S.; Becker, J.S. Laser ablation ICP-MS: Application in biomedical research. *Mass Spectrom. Rev.* **2017**, *36*, 47–57. [[CrossRef](#)]
28. Konz, I.; Fernández, B.; Fernández, M.L.; Pereiro, R.; González, H.; Álvarez, L.; Coca-Prados, M.; Sanz-Medel, A. Gold internal standard correction for elemental imaging of soft tissue sections by LA-ICP-MS: Element distribution in eye microstructures. *Anal. Bioanal. Chem.* **2013**, *405*, 3091–3096. [[CrossRef](#)]
29. Fernández, B. Elemental and molecular imaging by LA-ICP-MS. *Anal. Bioanal. Chem.* **2019**, *411*, 547–548. [[CrossRef](#)] [[PubMed](#)]
30. Paunesku, T.; Vogt, S.; Maser, J.; Lai, B.; Woloschak, G. X-ray fluorescence microprobe imaging in biology and medicine. *J. Cell. Biochem.* **2006**, *99*, 1489–1502. [[CrossRef](#)]
31. Uo, M.; Wada, T.; Sugiyama, T. Applications of X-ray fluorescence analysis (XRF) to dental and medical specimens. *Jpn. Dent. Sci. Rev.* **2015**, *51*, 2–9. [[CrossRef](#)]
32. Kump, P.; Vogel-Mikuš, K. Quantification of 2D elemental distribution maps of intermediate-thick biological sections by low energy synchrotron μ -X-ray fluorescence spectrometry. *J. Instrum.* **2018**, *13*, C05014. [[CrossRef](#)]
33. Collingwood, J.F.; Adams, F. Chemical imaging analysis of the brain with X-ray methods. *Spectrochim. Acta Part B At. Spectrosc.* **2017**, *130*, 101–118. [[CrossRef](#)]
34. Kanngießler, B.; Malzer, W.; Pagels, M.; Lühl, L.; Weseloh, G. Three-dimensional micro-XRF under cryogenic conditions: A pilot experiment for spatially resolved trace analysis in biological specimens. *Anal. Bioanal. Chem.* **2007**, *389*, 1171–1176. [[CrossRef](#)] [[PubMed](#)]
35. Strelci, C.; Rauwolf, M.; Turyanskaya, A.; Ingerle, D.; Wobruschek, P. Elemental imaging of trace elements in bone samples using micro and nano-X-ray fluorescence spectrometry. *Appl. Radiat. Isot.* **2019**, *149*, 200–205. [[CrossRef](#)]
36. Ishii, K.; Sugimoto, A.; Tanaka, A.; Satoh, T.; Matsuyama, S.; Yamazaki, H.; Akama, C.; Amartivan, T.; Endoh, H.; Oishi, Y.; et al. Elemental analysis of cellular samples by in-air micro-PIXE. *Nucl. Instrum. Methods Phys. Res. B* **2001**, *181*, 448–453. [[CrossRef](#)]
37. Tylko, G.; Mesjasz-Przybyłowicz, J.; Przybyłowicz, W.J. In-vacuum micro-PIXE analysis of biological specimens in frozen-hydrated state. *Nucl. Instrum. Methods Phys. Res. B* **2007**, *260*, 141–148. [[CrossRef](#)]
38. Vogel-Mikuš, K.; Pongrac, P.; Pelicon, P. Micro-PIXE elemental mapping for ionome studies of crop plants. *Int. J. PIXE.* **2014**, *24*, 217–233. [[CrossRef](#)]
39. Ishii, K. PIXE and Its Applications to Elemental Analysis. *Quantum Beam Sci.* **2019**, *3*, 12. [[CrossRef](#)]

40. Mulware, S.J. Comparative Trace Elemental Analysis in Cancerous and Noncancerous Human Tissues Using PIXE. *J. Biophys.* **2013**, *2013*, 192026. [[CrossRef](#)]
41. Sakai, T.; Oikawa, M.; Sato, T.; Nagamine, T.; Moon, H.D.; Nakazato, K.; Suzuki, K. New in-air micro-PIXE system for biological applications. *Nucl. Instrum. Methods Phys. Res. B.* **2005**, *231*, 112–116. [[CrossRef](#)]
42. Neumann, E.K.; Djambazova, K.V.; Caprioli, R.M.; Spraggins, J.M. Multimodal Imaging Mass Spectrometry: Next Generation Molecular Mapping in Biology and Medicine. *J. Am. Soc. Mass Spectrom.* **2020**, *31*, 2401–2415. [[CrossRef](#)]
43. Buchberger, A.R.; DeLaney, K.; Johnson, J.; Li, L. Mass Spectrometry Imaging: A Review of Emerging Advancements and Future Insights. *Anal. Chem.* **2018**, *90*, 240–265. [[CrossRef](#)]
44. Dilmetz, B.A.; Lee, Y.-R.; Condina, M.R.; Briggs, M.; Young, C.; Desire, C.T.; Klingler-Hoffmann, M.; Hoffmann, P. Novel technical developments in mass spectrometry imaging in 2020: A mini review. *Anal. Sci. Adv.* **2021**, *2*, 225–237. [[CrossRef](#)]
45. Eberlin, L.S. DESI-MS Imaging of Lipids and Metabolites from Biological Samples. In *Mass Spectrometry in Metabolomics: Methods and Protocols*; Raftery, D., Ed.; Springer: New York, NY, USA, 2014; pp. 299–311.
46. Eberlin, L.S.; Ferreira, C.R.; Dill, A.L.; Ifa, D.R.; Cooks, R.G. Desorption electrospray ionization mass spectrometry for lipid characterization and biological tissue imaging. *Biochim. Biophys. Acta Mol. Cell Biol. Lipids.* **2011**, *1811*, 946–960. [[CrossRef](#)]
47. Wiseman, J.M.; Ifa, D.R.; Song, Q.; Cooks, R.G. Tissue Imaging at Atmospheric Pressure Using Desorption Electrospray Ionization (DESI) Mass Spectrometry. *Angew. Chem., Int. Ed. Engl.* **2006**, *45*, 7188–7192. [[CrossRef](#)] [[PubMed](#)]
48. Bennett, R.V.; Gamage, C.M.; Fernández, F.M. Imaging of Biological Tissues by Desorption Electrospray Ionization Mass Spectrometry. *J. Vis. Exp.* **2013**, *77*, e50575.
49. Strittmatter, N.; Moss, J.I.; Race, A.M.; Sutton, D.; Canales, J.R.; Ling, S.; Wong, E.; Wilson, J.; Smith, A.; Howes, C.; et al. Multimodal molecular imaging maps the correlation between tumor microenvironments and nanomedicine distribution. *Theranostics* **2022**, *12*, 2162–2174. [[CrossRef](#)]
50. Lee, P.Y.; Yeoh, Y.; Omar, N.; Pung, Y.-F.; Lim, L.C.; Low, T.Y. Molecular tissue profiling by MALDI imaging: Recent progress and applications in cancer research. *Crit. Rev. Clin. Lab Sci.* **2021**, *58*, 513–529. [[CrossRef](#)]
51. Harris, A.; Roseborough, A.; Mor, R.; Yeung, K.K.C.; Whitehead, S.N. Ganglioside Detection from Formalin-Fixed Human Brain Tissue Utilizing MALDI Imaging Mass Spectrometry. *J. Am. Soc. Mass Spectrom.* **2020**, *31*, 479–487. [[CrossRef](#)]
52. Hermann, J.; Noels, H.; Theelen, W.; Lellig, M.; Orth-Alampour, S.; Boor, P.; Jankowski, V.; Jankowski, J. Sample preparation of formalin-fixed paraffin-embedded tissue sections for MALDI-mass spectrometry imaging. *Anal. Bioanal. Chem.* **2020**, *412*, 1263–1275. [[CrossRef](#)]
53. Bowman, A.P.; Bogie, J.F.J.; Hendriks, J.J.A.; Haidar, M.; Belov, M.; Heeren, R.M.A.; Ellis, S.R. Evaluation of lipid coverage and high spatial resolution MALDI-imaging capabilities of oversampling combined with laser post-ionisation. *Anal. Bioanal. Chem.* **2020**, *412*, 2277–2289. [[CrossRef](#)]
54. Sämfors, S.; Fletcher, J.S. Lipid Diversity in Cells and Tissue Using Imaging SIMS. *Annu. Rev. Anal. Chem.* **2020**, *13*, 249–271. [[CrossRef](#)] [[PubMed](#)]
55. Van Nuffel, S.; Quatredeniens, M.; Pirkl, A.; Zakel, J.; Le Caer, J.-P.; Elie, N.; Vanbellingen, Q.P.; Dumas, S.J.; Nakhleh, M.K.; Ghigna, M.-R.; et al. Multimodal Imaging Mass Spectrometry to Identify Markers of Pulmonary Arterial Hypertension in Human Lung Tissue Using MALDI-ToF, ToF-SIMS, and Hybrid SIMS. *Anal. Chem.* **2020**, *92*, 12079–12087. [[CrossRef](#)] [[PubMed](#)]
56. Agüi-Gonzalez, P.; Jähne, S.; Phan, N.T.N. SIMS imaging in neurobiology and cell biology. *J. Anal. At. Spectrom.* **2019**, *34*, 1355–1368. [[CrossRef](#)]
57. Sämfors, S.; Ståhlman, M.; Klevstig, M.; Borén, J.; Fletcher, J.S. Localised lipid accumulation detected in infarcted mouse heart tissue using ToF-SIMS. *Int. J. Mass Spectrom.* **2019**, *437*, 77–86. [[CrossRef](#)]
58. Massonnet, P.; Heeren, R.M.A. A concise tutorial review of TOF-SIMS based molecular and cellular imaging. *J. Anal. At. Spectrom.* **2019**, *34*, 2217–2228. [[CrossRef](#)]
59. Illes-Toth, E.; Hale, O.J.; Hughes, J.W.; Strittmatter, N.; Rose, J.; Clayton, B.; Sargeant, R.; Jones, S.; Dannhorn, A.; Goodwin, R.J.A.; et al. Mass Spectrometry Detection and Imaging of a Non-Covalent Protein–Drug Complex in Tissue from Orally Dosed Rats. *Angew. Chem. Int. Ed. Engl.* **2022**, *61*, e202202075. [[PubMed](#)]
60. Qi, K.; Wu, L.; Liu, C.; Pan, Y. Recent Advances of Ambient Mass Spectrometry Imaging and Its Applications in Lipid and Metabolite Analysis. *Metabolites* **2021**, *11*, 780. [[CrossRef](#)]
61. Unsihuay, D.; Sanchez, D.M.; Laskin, J. Quantitative Mass Spectrometry Imaging of Biological Systems. *Annu. Rev. Phys. Chem.* **2021**, *72*, 307–329. [[CrossRef](#)] [[PubMed](#)]
62. Moore, K.L.; Lombi, E.; Zhao, F.-J.; Grovenor, C.R.M. Elemental imaging at the nanoscale: NanoSIMS and complementary techniques for element localisation in plants. *Anal. Bioanal. Chem.* **2012**, *402*, 3263–3273. [[CrossRef](#)]
63. Liu, H.; Chen, R.; Wang, J.; Chen, S.; Xiong, C.; Wang, J.; Hou, J.; He, Q.; Zhang, N.; Nie, Z.; et al. 1,5-Diaminonaphthalene Hydrochloride Assisted Laser Desorption/Ionization Mass Spectrometry Imaging of Small Molecules in Tissues Following Focal Cerebral Ischemia. *Anal. Chem.* **2014**, *86*, 10114–10121. [[CrossRef](#)]
64. de Jesus, J.M.; Costa, C.; Burton, A.; Palitsin, V.; Webb, R.; Taylor, A.; Nikula, C.; Dexter, A.; Kaya, F.; Chambers, M.; et al. Correlative Imaging of Trace Elements and Intact Molecular Species in a Single-Tissue Sample at the 50 μm Scale. *Anal. Chem.* **2021**, *93*, 13450–13458. [[CrossRef](#)] [[PubMed](#)]

65. Costa, C.; de Jesus, J.; Nikula, C.; Murta, T.; Grime, G.W.; Palitsin, V.; Webb, R.; Goodwin, R.J.A.; Bunch, J.; Bailey, M.J. Exploring New Methods to Study and Moderate Proton Beam Damage for Multimodal Imaging on a Single Tissue Section. *J. Am. Soc. Mass Spectrom.* **2022**, *33*, 2263–2272. [[CrossRef](#)]
66. Sans, M.; Feider, C.L.; Eberlin, L.S. Advances in mass spectrometry imaging coupled to ion mobility spectrometry for enhanced imaging of biological tissues. *Curr. Opin. Chem. Biol.* **2018**, *42*, 138–146. [[CrossRef](#)] [[PubMed](#)]
67. Lewis, H.-M.; Costa, C.; Dartois, V.; Kaya, F.; Chambers, M.; de Jesus, J.; Palitsin, V.; Webb, R.; Bailey, M.J. Colocation of Lipids, Drugs, and Metal Biomarkers Using Spatially Resolved Lipidomics with Elemental Mapping. *Anal. Chem.* **2022**, *94*, 11798–11806. [[CrossRef](#)]
68. Swales, J.G.; Strittmatter, N.; Tucker, J.W.; Clench, M.R.; Webborn, P.J.H.; Goodwin, R.J.A. Spatial Quantitation of Drugs in tissues using Liquid Extraction Surface Analysis Mass Spectrometry Imaging. *Sci. Rep.* **2016**, *6*, 37648. [[CrossRef](#)]
69. Subbian, S.; Tsenova, L.; Yang, G.; O'Brien, P.; Parsons, S.; Peixoto, B.; Taylor, L.; Fallows, D.; Kaplan, G. Chronic pulmonary cavitary tuberculosis in rabbits: A failed host immune response. *Open Biol.* **2011**, *1*, 110016. [[CrossRef](#)] [[PubMed](#)]
70. Lamont, E.A.; Dillon, N.A.; Baughn, A.D. The Bewildering Antitubercular Action of Pyrazinamide. *Microbiol. Mol. Biol. Rev.* **2020**, *84*. [[CrossRef](#)] [[PubMed](#)]
71. Zimmerman, M.; Blanc, L.; Chen, P.-Y.; Dartois, V.; Prideaux, B. Spatial Quantification of Drugs in Pulmonary Tuberculosis Lesions by Laser Capture Microdissection Liquid Chromatography Mass Spectrometry (LCM-LC/MS). *J. Vis. Exp.* **2018**, *134*, e57402.
72. Chambers, M.C.; Maclean, B.; Burke, R.; Amodei, D.; Ruderman, D.L.; Neumann, S.; Gatto, L.; Fischer, B.; Pratt, B.; Egertson, J.; et al. A cross-platform toolkit for mass spectrometry and proteomics. *Nat. Biotechnol.* **2012**, *30*, 918–920. [[CrossRef](#)]
73. Race, A.M.; Styles, I.B.; Bunch, J. Inclusive sharing of mass spectrometry imaging data requires a converter for all. *J. Proteom.* **2012**, *75*, 5111–5112. [[CrossRef](#)] [[PubMed](#)]
74. Race, A.M.; Palmer, A.D.; Dexter, A.; Steven, R.T.; Styles, I.B.; Bunch, J. SpectralAnalysis: Software for the Masses. *Anal. Chem.* **2016**, *88*, 9451–9458. [[CrossRef](#)] [[PubMed](#)]
75. Wishart, D.S.; Feunang, Y.D.; Marcu, A.; Guo, A.C.; Liang, K.; Vázquez-Fresno, R.; Sajed, T.; Johnson, D.; Li, C.; Karu, N.; et al. HMDB 4.0: The human metabolome database for 2018. *Nucleic Acids Res.* **2018**, *46*, D608–D617. [[CrossRef](#)] [[PubMed](#)]
76. Grime, G.W.; Zeldin, O.B.; Snell, M.E.; Lowe, E.D.; Hunt, J.F.; Montelione, G.T.; Tong, L.; Snell, E.H.; Garman, E.F. High-Throughput PIXE as an Essential Quantitative Assay for Accurate Metalloprotein Structural Analysis: Development and Application. *J. Am. Soc. Mass Spectrom.* **2020**, *142*, 185–197. [[CrossRef](#)]
77. Patra, M.; Salonen, E.; Terama, E.; Vattulainen, I.; Faller, R.; Lee, B.W.; Holopainen, J.; Karttunen, M. Under the Influence of Alcohol: The Effect of Ethanol and Methanol on Lipid Bilayers. *Biophys. J.* **2006**, *90*, 1121–1135. [[CrossRef](#)]
78. Yin, R.; Burnum-Johnson, K.E.; Sun, X.; Dey, S.K.; Laskin, J. High spatial resolution imaging of biological tissues using nanospray desorption electrospray ionization mass spectrometry. *Nat. Protoc.* **2019**, *14*, 3445–3470. [[CrossRef](#)] [[PubMed](#)]

Disclaimer/Publisher's Note: The statements, opinions and data contained in all publications are solely those of the individual author(s) and contributor(s) and not of MDPI and/or the editor(s). MDPI and/or the editor(s) disclaim responsibility for any injury to people or property resulting from any ideas, methods, instructions or products referred to in the content.